Supporting Information

Reprogrammable, Magnetically Controlled Polymeric Nanocomposite Actuators

Li Wang[a,b,#], *Muhammad Yasar Razzaq*[a,#], *Tobias Rudolph*[a], *Matthias Heuchel*[a], *Ulrich Nöchel*[a], *Ulrich Mansfeld*[a], *Yi Jiang*[a,b], *Oliver E. C. Gould*[a], *Marc Behl*[a], *Karl Kratz*[a], *Andreas Lendlein*[a,b]*

[a]Institute of Biomaterial Science, Helmholtz-Zentrum Geesthacht, Kantstr. 55, 14513 Teltow, Germany;
[b]Institute of Chemistry, University of Potsdam, 14476 Potsdam, Germany
[#] authors contributed equally
*corresponding author: andreas.lendlein@hzg.de

1. Magnetic Actuator Preparation and Physico-chemical Characterization

1.1 Experimental

Star-shaped oligomer synthesis. The 4-arm star-shaped oligomeric ε-caprolactone (stOCL) with a M_n = 8300 g·mol^{-1} and 3-arm star-shaped oligomeric ω-pentadecalactone (stOPDL) with a M_n = 3400 g·mol^{-1} (containing hydroxy endgroups at each arm) were synthesized by ring-opening polymerization (ROP) of ε-caprolactone or ω-pentadecalactone and the respective tri- and tetra-functional initiators according to the method described elsewhere.[1]

Synthesis of coated magnetic nanoparticles. Oligomeric (ε-caprolactone) as well as oligomeric ω-pentadecalactone modified magnetic iron oxide nanoparticles (mNP-OCL and mNP-OPDL) were synthesized by surface-initiated ROP of magnetite mNPs obtained from co-precipitation as previously described.[2] The inorganic core of both mNP-OCL and mNP-OPDL had an average diameter of 12 ± 3 nm (analyzed by TEM). To determine the number average molecular weight (M_n) of grafted OCL or OPDL chains, polymer chains were detached by dissolving the inorganic core under acidic conditions. The obtained M_n values for the detached OCL was 1300 g·mol^{-1} (PDI = 2.3) and for detached OPDL was 2500 g·mol^{-1} (PDI = 3.1) as determined by size exclusion chromatography (SEC).[2] Based on the TGA results, the number of hydroxy groups per particle (n_{OH}) were calculated by equation S2, resulting n_{OH} = 270±50 for OCL and n_{OH} = 330±60 for OPDL, respectively.

Nanocomposite synthesis. Nanocomposites with different composition and nanoparticle dispersion were synthesized. In the following, the synthesis of samples containing a weight ratio of 15 wt% stOPDL and 85 wt% stOCL in the starting reaction mixture is described. Nanocomposites were synthesized by dissolving 5.45 g (0.66 mmol) stOCL, 0.95 g (0.28 mmol) stOPDL, and 0.7 g mNP-OCL (or mixture of 50 wt% mNP-OCL and 50 wt% mNP-OPDL which was pre-mixed with mortar and pestle) in a four-necked round bottom flask in 20 mL dichloromethane (CH_2Cl_2). After 10 min, 5 µL (8.4 µmol) of dibutyltin dilaurate (DBTL) and 0.5 mL hexamethylene diisocyanate (HDI) (3.1 mmol) were added to the reaction mixture, which was stirred vigorously at 300 rpm (Heidolph, RZR2102, Schwabach, Germany) at 80 °C for 60 min. Afterwards the reaction mixture was poured into a circular Teflon® container for solvent evaporation over 5 days at 60 °C. Finally, the formed nanocomposite networks were cured at 100 °C in an oven for 24 h at 100 mbar.

Swelling experiments were performed to estimate the gel content (G) of network samples, by swelling and extraction with chloroform according to the previously reported method[1]. Hereby, G was calculated by eq. S1, as quotient of the mass of the dried, extracted sample m_d and the mass of the unextracted sample m_{iso}.

$$G = \frac{m_{\mathrm{d}}}{m_{\mathrm{iso}}} \cdot 100\% \qquad \text{(S1)}$$

Gel permeation chromatography (GPC) was used to determine the number average molecular weight (M_{n}) of the star-shaped precursors stOCL and stOPDL, as well as the detached OCL oligomer of mNP-OCL and detached OPDL oligomer of mNP-OPDL. The measurements by universal calibration were performed on a system consisting of a precolumn, two 300×8 mm^2 linear M (10 µ) SDV-columns (Polymer Standards Service GmbH, Mainz, Germany), a degasser DG-2080-53, a RI-1530 refractive index detector, an isocratic pump PU-1580, an automatic injector AS-1555 (all JASCO, Groß-Umstadt, Germany), and a viscosimeter T-60A detector (VISCOTEK, Houston TX, USA). Chloroform ($CHCl_3$) with 0.2 wt% methanol as internal standard was used as eluent at a flow rate of 1.0 mL·min^{-1} at room temperature. Molecular weight and dispersity calculations were performed using WINGPC 6.2 (PSS) SEC software (Polymer Standard Service, Mainz, Germany).

Thermogravimetric analysis (TGA) experiments were performed on a Netzsch TGA 204 Phoenix (Netzsch, Selb, Germany). All experiments were conducted with a constant heating rate of 10 K·min^{-1}. The nanocomposite samples were heated from 25 to 800 °C under N_2 atmosphere. Weight percentage of OCL in the overall organic part was determined by a mass loss in a temperature range from 225 to 375 °C and was corresponding to thermal decomposition of OCL,[3] while mass loss from 375 to 475 °C was attributed to the thermal decomposition of OPDL.[4] The remaining mass at temperatures above 700 °C was related to the inorganic core of the mNPs. The standard deviation was given according to the instrument error. The number of hydroxy groups (n_{OH}) on the surface of mNP-OCL was calculated according to

$$n_{OH} = \frac{N_A \cdot \rho \cdot \frac{4}{3}\pi \cdot r^3}{b \cdot \overline{M}_n} \qquad \text{(S2)}$$

where N_{A} is the Avogadro constant, ρ is the density of the mNPs, r is the average radius of the mNPs (determined by TEM), and b is the weight percentage of mNP core of the coated mNPs (determined from TGA), and M_n is the number average molecular weight of the detached oligomers from the coated mNPs (determined by SEC).

Differential scanning calorimetry (DSC) measurements were carried out on a Netzsch DSC 204 (Netzsch, Selb, Germany) with a constant heating and cooling rate of 10 K·min^{-1}. For non-programmed samples, the temperature ranges for the 1st and 2nd heating runs were from 25 to

150 ºC and from -100 to 150 ºC, respectively. Data from the 2nd heating and 1st cooling run were analyzed. The degree of crystallinity (DOC) was calculated from the obtained melting enthalpies (ΔH_m) according to eq. S3 with $\Delta H^0_{m,PCL} = 139.3\ \mathrm{J \cdot g^{-1}}$ for 100% crystalline PCL[5] and $\Delta H^0_{m,PPDL} = 233\ \mathrm{J \cdot g^{-1}}$ for 100% crystalline PPDL[6]. The standard deviation of T_m, T_c, and DOC was given according to the machine error.

$$\mathrm{DOC} = \frac{\Delta H_m}{\Delta H^0_m} \cdot 100\% \qquad \text{(S3)}$$

Tensile tests. The elongation at break (ε_b) of the nanocomposites was determined by tensile tests carried out with DIN EN ISO 1BB specimens on a Z005 tensile tester (Zwick, Ulm, Germany) at 100 °C. The strain rate was 10 mm·min^{-1}. Five measurements were conducted for each nanocomposite.

Scanning electron microscopy (SEM) was used to characterize the distribution of the mNP within the bulk material on the micrometer scale using a Gemini Supra 40 VP (Zeiss, Oberkochen, Germany) at 10 kV equipped with a back-scattered electron (BSE) detector. The bulk material was cut with a razor blade at room temperature perpendicular to the film surface and coated with carbon by a Polaron SC7640 sputter coater (Quorum technologies Ltd., Ashford, UK) and the coated cross sections were investigated at room temperature.

Transmission electron microscopy (TEM) was used to characterize the morphology of the coated mNP and the composite network samples. Investigations were performed at 200 kV and room temperature on a Talos F200X (FEI, Eindhoven, The Netherlands) with high-brightness electron source (X-FEG). The images were obtained with a CMOS technology based camera model Ceta 16M. mNP samples were prepared by dissolving a small amount of mNPs in 2 ml $CHCl_3$ and placed for 10 min in an ultrasonic bath at ambient temperature. The samples were allowed to settle overnight. A Lacey-carbon copper grid (Plano GmbH, Wetzlar, Germany, S166-4) was dipped into the supernatant and the residual chloroform was removed by filter paper. Finally, the samples were dried by evaporation at ambient conditions. The mean diameter of the mNP cores was determined by analyzing a large number of particles. The average thickness of the polymeric shell was measured at three different positions of five single particles with software Scandium (Version 5.2 Olympus Soft Imaging Solutions GmbH). For composite sample preparation, the materials were cut with a cryo-ultramicrotome (Leica EM FC6, Wetzlar, Germany) at -120 °C using a diamond knife. The obtained films with a cutting size of 150×150 μm^2 and a thickness of 50 to 100 nm were placed on a copper grid with 400 mesh size and was stored at ambient conditions overnight prior to measurements.

1.2 Nanocomposite Characteristics

High gel content (G) values up to 97±2% determined in swelling experiments with $CHCl_3$ indicated an almost complete conversion of the starting materials. Thermogravimetric analysis of the nanocomposite confirm the desired composition of OCL and OPDL of the organic part and approximately 4 wt% of inorganic moieties related to the mass of the magnetite nanoparticle's core in the nanocomposite. The elongation at break (ε_b) at 100 °C (in the complete rubbery-elastic state) of the composite network was determined to be above 50%. All data determined for the different composite materials are summarized in Tables S1-3.

Table S1. Composition of respective actuators

Composition of NCs	G^a (%)	ε^b (%)	*mNP content*^{c} (wt%)	*OCL*^{c} (wt%)	*OPDL*^{c} (wt%)
NC(85/15)-mNP-OCL	97±2	103±10	4.0±0.1	86.5±0.1	13.5±0.1
NC(85/15)-mNP-(OCL/OPDL)	84±2	73±10	4.1±0.1	85.2±0.1	14.8±0.1
NC(80/20)-mNP-OCL	95±2	115±10	4.3±0.1	81.3±0.1	18.7±0.1
NC(75/25)-mNP-OCL	97±2	52±10	4.1±0.1	76.7±0.1	23.3±0.1

a. Gel content obtained from swelling experiments
b. Elongation at break obtained from tensile test at 100 °C
c. mNP weight content of the networks and the weight percentage of OCL and OPDL in organic part characterized by TGA

Table S2. Thermal properties of respective actuators

Composition of NCs	$T_{c,OCL}^d$ (°C)	$DOC_{c,OCL}^e$ (%)	$T_{c,OPDL}^d$ (°C)	$DOC_{c,OPDL}^e$ (%)	$T_{m,OCL}^f$ (°C)	$DOC_{m,OCL}^g$ (%)	$T_{m,OPDL}^f$ (°C)	$DOC_{m,OPDL}^g$ (%)
NC(85/15)-mNP-OCL	20±1	34±1	60±1	7±1	53±1	27±1	84±1	4±1
NC(85/15)-mNP-(OCL/OPDL)	21±1	33±1	60±1	4±1	51±1	34±1	78±1	7±1
NC(80/20)-mNP-OCL	21±1	34±1	60±1	8±1	47±1	40±1	83±1	3±1
NC(75/25)-mNP-OCL	22±1	38±1	63±1	7±1	46±1	34±1	82±1	6±1

d. Crystallization temperature obtained from DSC, 1st cooling run data
e. Crystallinity in OCL/OPDL domains calculated from DSC, 1st cooling run data
f. Melting temperature obtained from DSC, 2nd heating run data
g. Crystallinity in OCL/OPDL domains calculated from DSC, 2nd heating run data

Table S3. Crystallinity of respective actuators

Composition of NCs	X_c^h *(%)*	l_c^h *(nm)*	X_c^i *(%)*	l_c^i *(nm)*
NC(85/15)-mNP-OCL	33±1	15.0±0.1	10±1	13.5±0.1
NC(85/15)-mNP-(OCL/OPDL)	-	-	-	-
NC(80/20)-mNP-OCL	37±1	16.2±0.1	5±1	15.4±0.1
NC(75/25)-mNP-OCL	32±1	16.0±0.1	18±1	16.2±0.1

h. Calculated crystallinity index and crystal size from WAXS at 25 °C after programming
i. Calculated crystallinity index and crystal size from WAXS at 60 °C at 1st cycle

DSC measurements between -100 and 150 °C of the nanocomposite revealed two separated melting temperatures ($T_{\mathrm{m,OCL}}$ ~ 53±1 °C, $T_{\mathrm{c,OPDL}}$ ~ 60±1 °C) and crystallization transitions ($T_{\mathrm{c,OCL}}$ ~ 21±1 °C and $T_{\mathrm{c,OPDL}}$ ~ 60±1 °C) indicating a phase-segregated morphology of the composite materials (Figure S1). From the data obtained in the DSC heating run a degree of crystallinity of $DOC_{\mathrm{m,OCL}}$ ~ 34-38±1% was calculated by eq. S3 for the OCL domains, while $DOC_{\mathrm{m,OPDL}}$ was ~ 4-7±1%. The obtained data are listed in Table S2.

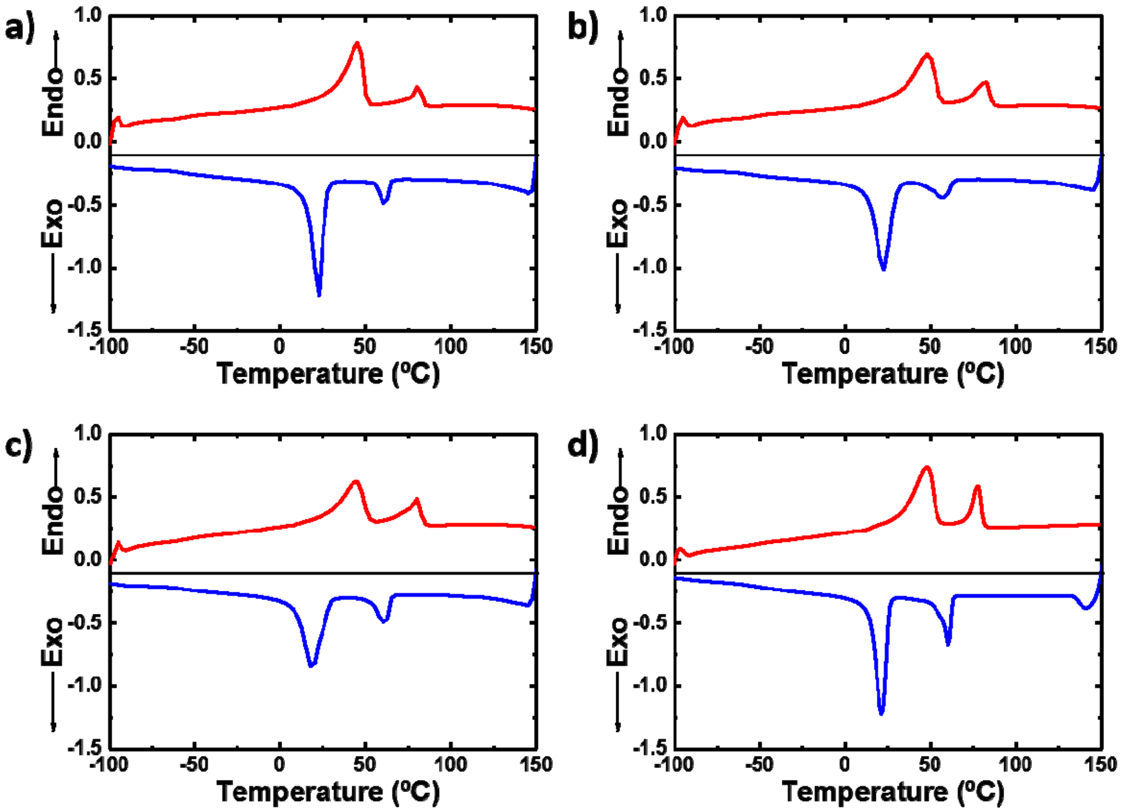

Figure S1. Comparison of DSC traces from the 2nd heating (red curves) and 1st cooling (blue curves) run of the nanocomposite sample: a) NC(85/15)-mNP-OCL, b) NC(80/20)-mNP-OCL, c) NC(75/25)-mNP-OCL, and d) NC(85/15)-mNP-(OCL/OPDL).

Bright-field TEM images of *mNP-OCL* showed crystalline iron oxide nanoparticles, which are surrounded by an amorphous layer supporting the successful modification with OCL (Figure S2a), that was reported previously.[2] The morphology of the original nanocomposite NC(85/15)-mNP-OCL/OPDL and NC(85/15)-mNP-OCL on the micro-scale level was elucidated by SEM. BSE images of cross sections showed micro-sized agglomerates of nanoparticles that were statistically distributed within the polymer matrix for both nanocomposites (Figure S2b,e). The micro-sized agglomeration was significantly pronounced in the case of NC(85/15)-mNP-OCL. The morphology was further characterized by TEM as displayed in Figure S2c, d, f, g. Bright-field imaging confirmed a phase-segregated domain structure of the polymer matrix, where the islands represent the OPDL phase embedded in the OCL phase. In case of NC(85/15)-mNP-OCL/OPDL the mNP were selectively located at the OPDL/OCL interfaces representing nano-sized agglomerates (Figure S2d). In contrast, the mNP in NC(85/15)-mNP-OCL are statistically distributed as pronounced single particles in the OCL phase (Figure S2g).

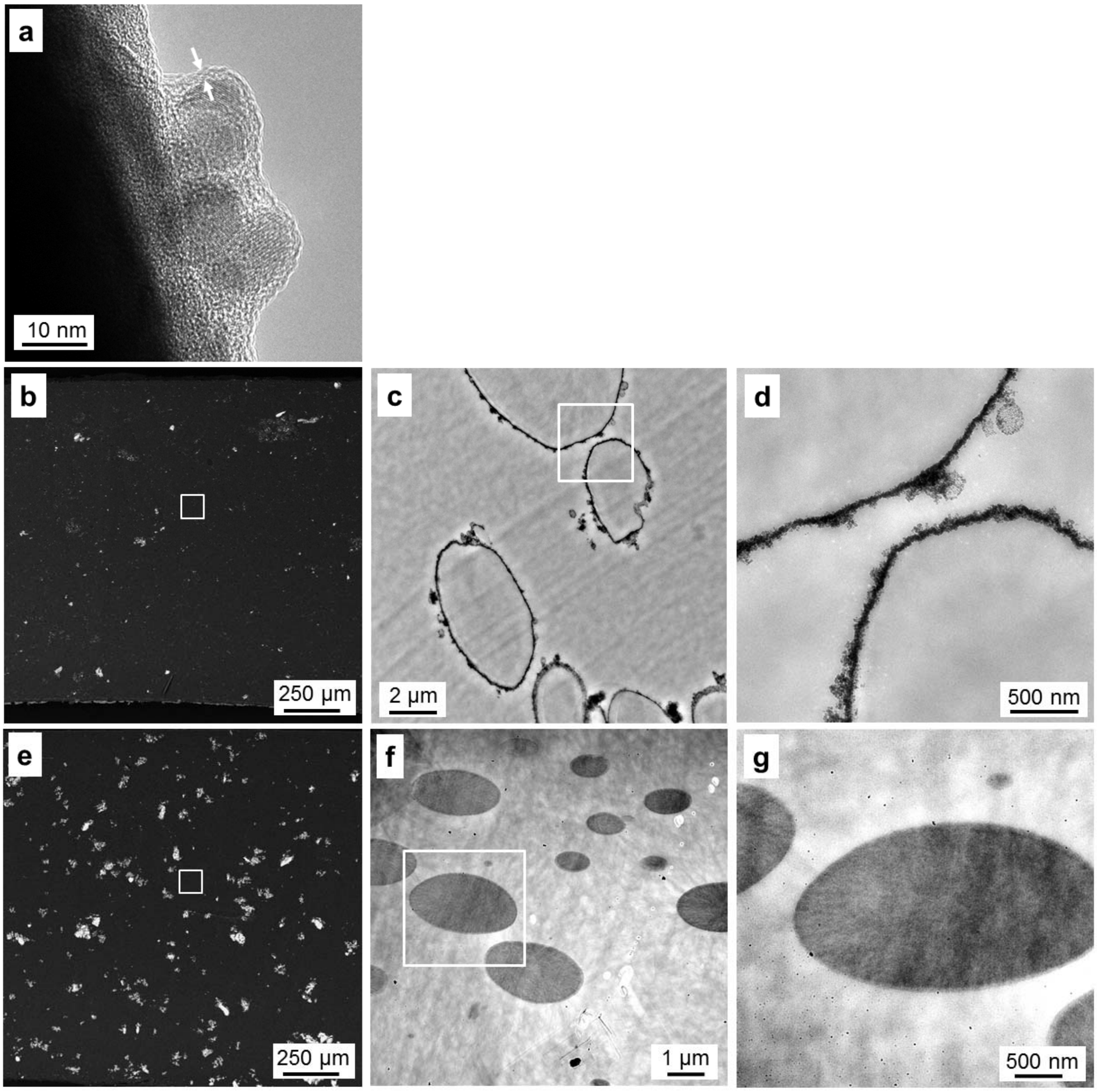

Figure S2. Electron micrographs of the mNP and nanocomposites: a) The bright-field TEM image of mNP-OCL shows nanoparticles coated with an amorphous layer of a thickness roughly indicated by the white arrows. The SEM image represent cross sections of the NC(85/15)-mNP-OCL/OPDL (b) and NC(85/15)-mNP-OCL (e) bulk material showing large agglomerates of the mNP-OCL/OPDL and mNP-OCL/OPDL nanoparticles (bright spots), respectively, that are statistically distributed within the polymer material (dark matrix). The white rectangles locate the areas where TEM foils were cut from. Bright-field TEM images in c) and d) represent the polymer composite material with OPDL islands in the OCL matrix with the mNP (black dots) located selectively at the polymer interfaces. Bright-field TEM images in f) and g) represent the polymer composite material with OPDL (dark) islands in the OCL matrix and statistically distributed mNP (black dots) that are selectively located in the OCL phase. To visualize the OPDL islands, a large contrast difference between OCL and OPDL was produced by using a small objective aperture and a large underfocus. The white rectangles in c) and f) represent the areas of magnification for d) and g), respectively.

2. Analysis of Thermally Initiated Actuation Function

2.1 Experimental

Cyclic thermomechanical testing experiments. Reversible actuation was quantified by cyclic, thermomechanical tensile tests with a standardized sample shape (ISO 527–2/1BB) on a Zwick Z1.0 machine (Zwick, Ulm, Germany) equipped with a thermo-chamber and temperature controller (Eurotherm Regler, Limburg, Germany). The experiment consisted of an initial programming cycle and three subsequent reversible actuation cycles. A single step programming procedure was applied, where the sample was stretched with a rate of 10 mm·min^{-1} to 50% strain at T_{prog} (which is correlating with the temperature achieved at H_{reset}) followed by an equilibration time of 5 min and cooling below crystallization temperature (0 °C) under constant strain. After another 5 min equilibration time, the stress was released to zero at this lower temperature and the sample was reheated to T_{high} (which is correlating with the temperature obtained at H_{high}) under stress-free conditions. The reversible actuation cycles consisted of continuous heating/cooling runs at a constant rate from T_{low} to T_{high}, including 5 min waiting time at T_{low} and T_{high}. Relative reversible elongation $\varepsilon_{\mathrm{rev}}$ and the fixation efficiency Q_{ef} were calculated according to equations S4 and S5:

$$\varepsilon_{rev} = \frac{\varepsilon_{\mathrm{B}} - \varepsilon_{\mathrm{A}}}{1 + \varepsilon_{\mathrm{A}}} \cdot 100\% \qquad \text{(S4)}$$

$$Q_{ef} = \frac{\varepsilon_{A}}{\varepsilon_{prog}} \cdot 100\% \qquad \text{(S5)}$$

Atomic force microscopy (AFM) experiments with a programmed sample (elongation of 30%, 50 μm thickness by microtome cutting) were performed on an AFM instrument (MFP-3D, Asylum Research, California, USA) in AC mode. The temperature was controlled using a temperature controller (Asylum Research, California, USA) equipped with a Peltier element. The typical scan rate was 0.5 Hz. A silicon cantilever (OMCL AC240TS-R3, Olympus, Tokyo, Japan), having a driving frequency of around 150 kHz and a spring constant of 9 N·m^{-1}, was used. The tip had a radius of 7 nm, while the tip back and side angles were 35° and 18°, respectively. The surfaces with thickness of 50 μm were glued on an iron plate, which was mounted on an AFM sample holder. The nanocomposite sample was repetitively heated to 60 ºC and cooled to 25 ºC with a rate of 10 °C·min^{-1}. The surfaces were kept at each temperature (60 or 25 ºC) at least for 10 min before scanning, ensuring the melting or crystallization of the OCL domains. The AFM images were analyzed by ImageJ by measuring the distance of OPDL droplet like structures at 60 °C (D_{A}) and at 25 °C (D_{B}). The reversible change in distance (D_{rev}) was calculated according to eq. S6

$$D_{rev} = \frac{D_{\mathrm{B}} - D_{\mathrm{A}}}{D_{\mathrm{A}}} \cdot 100\% \qquad \text{(S6)}$$

Wide angle X-ray scattering (WAXS) measurements on programmed samples (elongation of 30%) were conducted at ambient temperature and 60 °C utilizing an X-ray diffraction system D8 Discover with a two-dimensional HI-Star detector from Bruker AXS (Bruker, Karlsruhe, Germany) in transmission geometry. The distance sample - detector was 150 mm and the wavelength $\lambda = 0.154$ nm. Integration of the two-dimensional isotropic patterns resulted into one-dimensional scattering curves for analysis (I *vs* 2θ). The peaks of the two phases (amorphous and crystalline) were fitted with Pearson VII functions. The relationship of the integrated areas determines the crystallinity index (X_c) (eq. S7). The relation of the peak position and full width at half maximum (FWHM) with the average crystal size (l_c) is given by the Sherrer equation (S8). The standard deviation of the X_c and l_c was given according to the machine error.

$$X_c = \frac{A_{cryst}}{A_{cryst} + A_{amorph}} * 100 \qquad \text{(S7)}$$

$$l_c = \frac{k \cdot \lambda}{\mathrm{B} \cdot \cos\theta} \qquad \text{(S8)}$$

where B = FWHM (in radians), θ = half scattering angle, λ = wavelength of X-rays. l_c was determined from the main diffraction peak around $2\theta \approx 21.5°$, which can be attributed to the 110 planes of the orthorhombic crystal structure of PCL as well as PPDL.[7]

2.2. Thermal Actuation Behavior

To determine the reversible shape-memory actuation capability of the nanocomposite, cyclic uniaxial thermomechanical experiments were performed in a thermochamber (without applying any alternating magnetic field, AMF). The samples were programmed to 50% strain at 100 °C before fixation at 0 °C. The reversibility of actuation is recorded under stress-free conditions for at least 3 cycles. Figure S3 shows the reversible actuation resulting in melt-induced contraction and crystallization-induced elongation of the specimens during the heating/cooling cycle. Here, the determined values are for NC(85/15)-mNP-OCL $\varepsilon_{\mathrm{rev}} = 5.6 \pm 0.1\%$, NC(80/20)-mNP-OCL $\varepsilon_{\mathrm{rev}} = 5.1 \pm 0.1\%$, NC(75/25)-mNP-OCL of $\varepsilon_{\mathrm{rev}} = 2.3 \pm 0.1\%$, NC(85/15)-mNP-(OCL/OPDL) of $\varepsilon_{\mathrm{rev}} = 5.3 \pm 0.1\%$, and $\varepsilon_{\mathrm{rev}} = 6.1 \pm 0.1\%$ for the pure multiphase copolymer network.

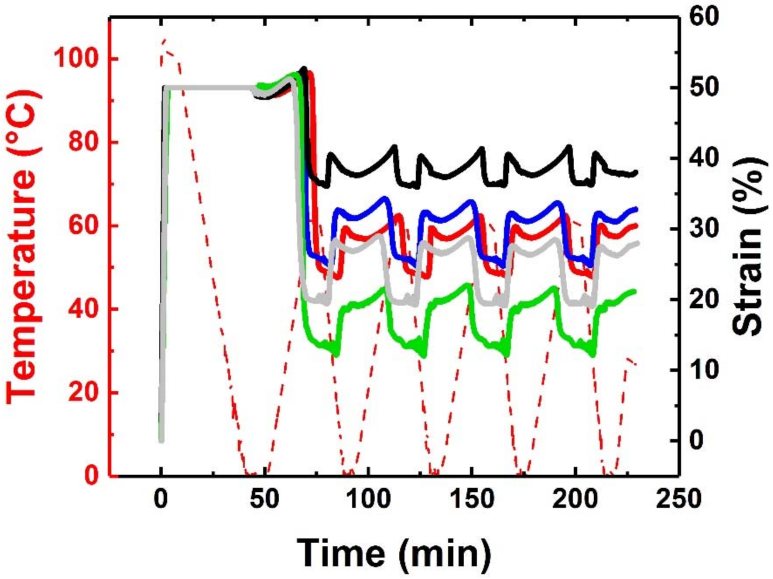

Figure S3. Comparison of cyclic test results of different nanocomposites and pure multiphase copolymer network with T_{prog} = 100 °C, $\varepsilon_{\mathrm{prog}}$ = 50%, T_{low} = 0 °C, and T_{high} = 60 °C, a heating rate of 3 K·min^{-1} and a cooling rate of 3 K·min^{-1}. NC(85/15)-mNP-OCL (blue curve), NC(80/20)-mNP-OCL (red curve), NC(75/25)-mNP-OCL (black curve), NC(85/15)-mNP-(OCL/OPDL) (green curve), and pure multiphase copolymer network (85/15) (grey curve).

Furthermore, AFM experiments conducted with programmed samples at ambient temperature confirmed the multiphase morphology of the nanocomposite on the micro level, where ellipsoidal OPDL islands are distributed in the OCL matrix (Figure S4i). The OPDL islands size ranges between 1.0±0.2 µm and 5.0±0.2 µm. Representative AFM phase images obtained during two subsequent heating cooling cycles between 60 °C and 25 °C (thermal actuation) of a programmed nanocomposite sample are displayed in Figure S4. D_{rev} was calculated according to eq. S6 based on the changes in the distance of the centers of the OPDL droplets during thermal actuation. Here, a D_{rev} of 4.4±0.1% was obtained in the first actuation cycle, while a lower value of 2.7±0.1% was found in the second cycle. These microscopic shape changes are in agreement with the reversible strains observed in magneto-mechanical experiments.

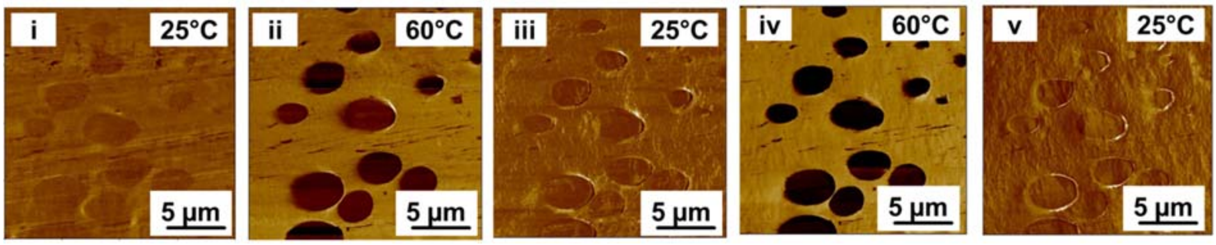

Figure S4. AFM images of a nanocomposite sample programmed by elongation to ε = 50% before thermally induced actuation (i) and picture series of two thermal actuation cycles obtained by repetitive heating to 60 °C and cooling to 25 °C (ii-v).

The changes in the crystalline nanostructure during thermal actuation of a programmed sample (elongated with ε_{prog} = 50%) were followed by WAXS measurements. Representative 2D WAXS patterns and the related intensity scattering profiles obtained in subsequent heating-cooling cycles are shown in Figures S5a, b. The strongest reflections were related to the (110) and (200) reflections of both OCL and OPDL crystals (Figures S5a, i). The sickle-like reflections indicated anisotropic crystal orientation, demonstrating that a certain preferential orientation occurred within both crystals after programming. The maximum of the (110) reflection was found on the equator, indicating orientation of the molecular chains (crystal c-axis) parallel to the direction of deformation. After increasing the temperature to 60 °C (OCL in the melt) the peak intensity decreased and can be solely attributed to the crystalline OPDL signals. The crystallinity index at 60 °C ($X_{c,OPDL}$) was around 8% (Table S1), which was in good agreement with the corresponding DSC data. After cooling to 25 °C, the peak intensity increased again, caused by the newly formed OCL crystals (Figures S5a, ii-v). The overall crystallinity index obtained after the first actuation cycle was around 5% lower than that determined for the samples after programming, which can be attributed to the short cooling period during the cyclic experiments. The average lateral crystal size (l_c) was found between 17.0±0.1 nm to 17.4±0.1 nm and did not significantly vary during heating and cooling (Table S1). From the azimuthal (radial) profiles of the strongest peak, i.e. the (110) reflection, attributed to OCL and OPDL at 25 °C and only to OPDL at 60 °C (where OCL is completely amorphous), plots of intensity vs. radial angle were produced (Figure S5c). The full width at half maximum (FWHM) indicates the degree of crystal orientation and was found to be ~75° (in chi) at 60 °C and around 60° (in chi) at 25 °C, reflecting the oriented crystallization of the OCL actuation domain.

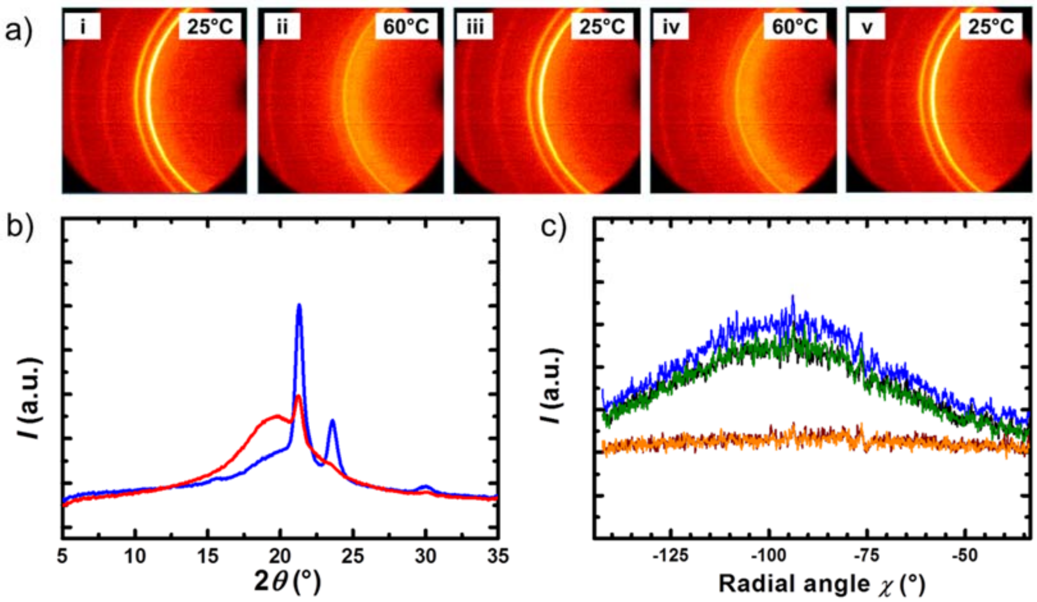

Figure S5. a) WAXS pattern of a nanocomposite sample programmed by elongation to ε = 30% (i) at 25 °C before thermal actuation and WAXS pattern series of two actuation cycles obtained by repetitive heating to 60 °C and cooling to 25 °C (i-v). b) WAXS scattering intensity profiles of the first thermal actuation cycle at 60 °C (red) and 25 °C (blue). c) Azimuthal plot with radial angle χ after programming (blue), 1st cooling to 25 °C (black), 1st heating to 60 °C (orange), 2nd cooling to 25 °C (green) and 2nd heating to 60 °C (dark red).

3. Analysis of Magnetic Heating Function

3.1 Experimental

Magnetic heating experiments: a composite network test specimen (20×2×1 mm^3) was positioned in an AMF at a frequency of f = 258 *k*Hz. By adjusting the generator power output, different magnetic field strength (H) values were selected and the heating behavior of the composite was observed, whereby T was recorded by an infrared video camera VarioCAM® HiRes (InfraTec GmbH, Dresden, Germany) over a time of 300 seconds (Figure S6).

Based on the assumption that the temperature gradient within the sample becomes vanishingly small within the first second, spatial variation of temperature can be ignored, and the time dependent average temperature $T(t)$ can be fitted with a model[8] (eq. S9) depending on a system time constant τ, the environmental temperature T_{env} and an effective heat generation constant $\bar{P}$ in the composite.

$$T(t) = \bar{P}\tau\left(1 - e^{-\frac{t}{\tau}}\right) + T_{\text{env}} \qquad \text{(S9)}$$

The model interprets the time constant as $\tau = \rho C_P V / hA$, were ρ is the density, C_P the heat capacity, V and A are volume and surface area of the (cylindrical) sample and h is the convective heat transfer coefficient of the surrounding air. The effective heat generation constant $\overline{P} = S_M / \rho C_P$ is proportional to S_M, the rate of heat generation per unit volume of the composite sample. The predicted fit values for effective heat generation constant $\bar{P}$ and time constant τ depending on the selected field strength H are summarized in Table S4.

3.2 Magnetic Heating Behavior

Inductive heating experiments in an AMF at H = 12.1 kA·m^{-1} revealed an achievable temperature of 60±1 °C for NC(85/15)-mNP-OCL, while a lower plateau temperature of 50 ±1 °C was obtained for NC(85/15)-mNP-(OCL/OPDL). Increasing the magnetic field strength from H_{low} = 10.0 kA·m^{-1} to H_{reset} = 30.0 kA·m^{-1} resulted in an increase in achievable surface temperature for NC(85/15)-mNP-OCL recorded by the infrared video camera from 37±1 °C to 88±1 °C (Figure S6). The effective heat generation constant $\bar{P}$ (resulting from the curve fittings according to eq. S9) increase as well with increasing H from 0.315±0.004 K·s^{-1} to 1.930±0.015 K·s^{-1}, while the system time constant τ decreased with increasing H from 48.5±0.7 s to 32.4±0.3 s (Table S4). In this way, the applied magnetic field strength is a suitable parameter to control the inductive heating capability of such nanocomposites.

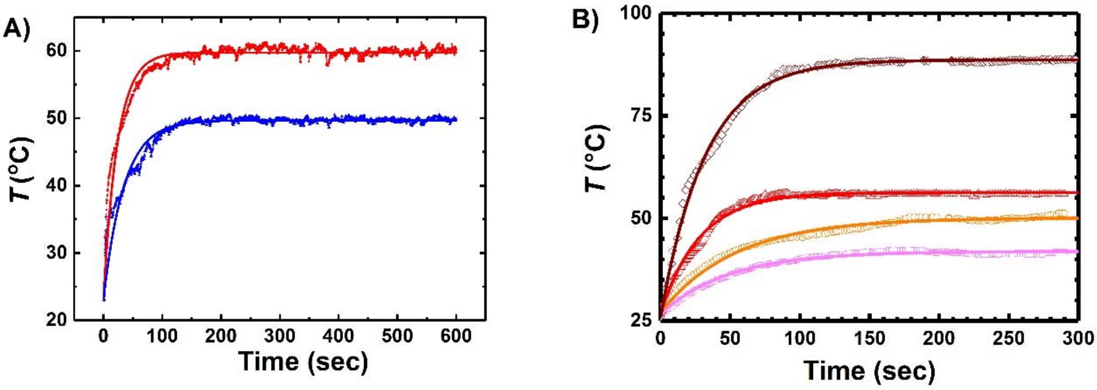

Figure S6. Time dependent average temperature change of nanocomposites and respective curve fittings according to eq. S9 as solid lines. A) Comparison of development of temperature during magnetic heating at H = 12.1 kA·m^{-1} for NC(85/15)-mNP-OCL (red symbols and red line) and NC(85/15)-mNP-(OCL/OPDL) (blue symbols and blue line). B) Temperature of NC(85/15)-mNP-OCL during magnetic heating experiments in an AMF of different field strength H: H_{low} = 10.0 kA·m^{-1} (open squares, light magenta line); H_{mid} = 10.5 kA·m^{-1} (open circle, orange line); H_{high} = 11.2 kA·m^{-1} (open triangle, red line); H_{reset} = 30.0 kA·m^{-1} (open diamond, dark red line).

Table S4. Magnetic heating properties of nanocomposite at different H

H[a] (kA·m^{-1})	$\overline{P}$[b] (K·s^{-1})	τ[c] (s)	T[d] (° C)
10.0	0.315±0.004	48.5±0.7	37±1
10.5	0.425±0.006	54.0±0.9	45±1
11.2	1.044±0.010	28.2±0.3	57±1
30.0	1.930±0.015	32.4±0.3	88±1

a. Magnetic field strengths used during magnetic heating experiments.
b. Effective heat generation constant $\overline{P}$, see eq. S9
c. Time constant τ, see eq. S9
d. Surface temperature

3.3 Cooling Behavior after Removing Magnetic Field

The temporal surface temperature change $T_{\mathrm{surf}}(t)$ of a composite network test specimen (20×2×1 mm^3) was observed after the AMF was switched off, i.e. at H = 0 kA·m^{-1}. The thermal cooling took place in a surrounding temperature of 25 °C. T was recorded by an infrared video camera VarioCAM® HiRes (InfraTec GmbH, Dresden, Germany) over a time of 300 seconds. For the first 150 seconds, Figure S7 presents (interpolated) temperature data in the cooling phase, i.e. after the previous heating step (at different field strength) was completed by switching off the magnetic field.

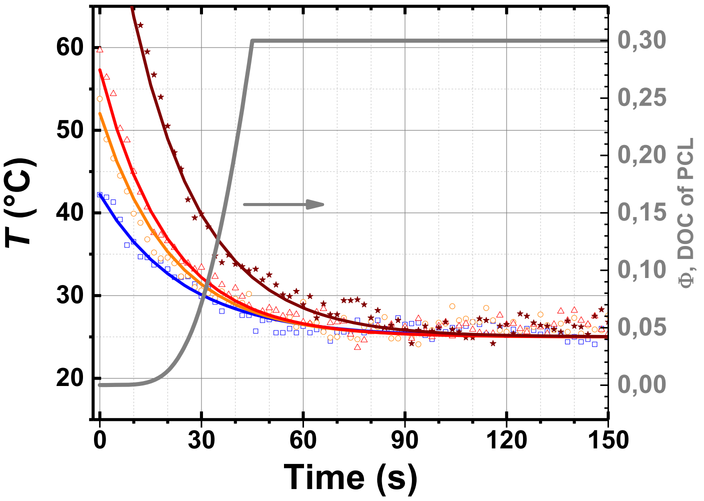

Figure S7. Thermal cooling curves of NC-mNP-OCL, after magnetic heating steps at different field strength H, indicated by temporal surface temperature data and respective curve fittings according to eq. 10 as solid lines: H = 10.0 kA·m^{-1} (open squares, blue line); H = 10.5 kA·m^{-1} (open circle, orange line); H = 11.2 kA·m^{-1} (open triangle, red line) and H = 30.0 kA·m^{-1} (solid stars, brown line). The gray line represents a prediction of temporal PCL crystallization during cooling after magnetic heating at H = 11.2 kA·m^{-1}.

The T-data of the thermal cooling processes can be fitted with an exponential decay equation (eq. S10):

$$T(t) = A * \exp\left(-\frac{t}{\tau}\right) + T_{RT} \qquad \text{(S10)}$$

The fit parameters are presented in Table S5. The fit parameter $A = T_{t=0} - T_{RT}$ corresponds to the initial T-difference between sample and surrounding. The parameter τ presents the characteristic time constant of the cooling process. It can be interpreted as $\tau = mC_p/hA$, i.e. the ratio out of the product of mass m times mass-specific heat capacity C_p and the product of heat transfer coefficient h and the heat transfer surface area A.

Table S5. Fit parameters (see eq. S10) for thermal cooling processes following on magnetic heating steps at different magnetic field strength.

H[a] (kA·m^{-1})	A[b] (°C)	τ[c] (s)
10.0	17.2±0.5	24.6±1.2
10.5	27.0±1.1	20.7±1.4
11.2	32.3±1.1	20.0±1.1
30.0	62.6±1.2	20.8±0.6

a. Magnetic field strength of AMF used during preceding magnetic heating step
b. $A = T_{t=0} - T_{RT}$ initial T-difference between sample and surrounding
c. Time constant, see eq. S10

The characteristic time constants of the thermal cooling processes after magnetic heating steps at field strength of 10.5 to 30 kA·m^{-1} agree well in range of errors, indicating the same universal cooling process of the sample, starting only from different initial temperatures. A slightly higher value was found for the lowest field strength H = 10.0 kA·m^{-1}.

Figure S7 contains also a model-like prediction of the crystallization of an initially molten OCL-domain. The starting point is the experimental data set of crystallization half time values $t_{1/2}$ of PCL at different temperatures.[9] At 55 °C the $t_{1/2}$- value is over 10^5 s, and for 25 °C it is only about $t_{1/2}$ ~ 5 s. A numerical fit of these $t_{1/2}$-data in the T-range of 20 to 55 °C was used to calculate numerically (stepwise in 1 s-steps) the increasing crystallization, starting from the molten OCL-domains (DOC $\Phi \leq 0.0001$) up to a maximum *DOC*-value of $\Phi = 0.3$. The gray curve in Figure S7 shows the temporal progress of the crystallization during the cooling process after a magnetic heating step with H_{high} = 11.2 kA·m^{-1}. The crystallization process starts notable after about 15 s, when the actuator sample has a temperature of about 37 °C. After about 40 s, when T is about 30 °C half of the crystals in the OCL-domains are formed, and after ~45 s, at T ~ 28 °C the crystallization process is finished.

4. Magnetic Triggering of the Nanocomposite Actuators

4.1 Experimental

Experimental setup for multi-ring measurements. For the fabrication of a multi-ring specimen a film ($40\times2\times1$ mm^3) was heated up to 100 °C in a water bath and bent around a stick with a diameter of 6 mm for 2 minutes. The resulting multi-ring was obtained after fixation by cooling in an ice-bath. For the analysis of the multi-ring experiment, the distance (d) of the ring in the middle between the closing/contacting points was chosen for comparison and analysis as illustrated in Figure S11.

Magnetically controlled actuation experiments: Initial programming of the composite networks test specimen ($20\times2\times1$ mm^3) was performed by bending the originally straight sample $\theta = 0°$ to a temporal angle $\theta = 180°$ at 100 °C by folding to a hairpin like shape and cooling to ambient temperature for fixation. With such programmed (bended) samples different kinds of actuation experiments were conducted. In a first set of experiments the magnetic field was switched on and off, whereby different magnetic field strengths H ranging from $H = 8.5$ kA m^{-1} to $H_{\mathrm{high}} =$ 11.2 kA·m^{-1} were applied for 2 minutes to reach bending angle θ_{A} and afterwards the AMF was switched off ($H_{\mathrm{off}} = 0$ kA m^{-1}) for 2 minutes to reach bending angle θ_{B}. Variation of the exposure time periods (t) applied for both H and H_{off} in the range from 50 s to 10 min represents the second type of actuation experiments. A third set of actuation experiments consisted of stepwise increasing and decreasing the magnetic field strength between $H_{\mathrm{off}} = 0$ kA m^{-1} and $H_{\mathrm{high}} = 11.2$ kA·m^{-1} in three repetitive cycles. Here, each H-value was kept constant for 2 min before increasing or decreasing H.

After erasing the bending actuation geometry of the test specimen by application of $H_{\mathrm{reset}} =$ 30 kA·m^{-1} or 100 °C the same sample was reprogrammed to a concertina-like shape (alternatively clip or ring shaped) consisting of four 180° hairpins at 100 °C. With such concertina-like shape the change in length L was monitored during stepwise increasing and decreasing the magnetic field strength between $H_{\mathrm{off}} = 0$ kA m^{-1} (L_{B}) to $H_{\mathrm{high}} = 11.2$ kA·m^{-1} (L_{A}) in three repetitive cycles. Here each H-value was kept constant for 2 min before increasing or decreasing H. At least three repeating magnetic actuation cycles were performed in all experiments. The change of bending angles or length of the concertina-like specimen was observed by a digital camera (Canon NEGRIA, Tokyo, Japan) and analyzed by ImageJ software, while an infrared video camera VarioCAM® HiRes (InfraTec GmbH, Dresden, Germany) was used to record the achieved temperatures.

Fixation efficiency after programming by bending (Q_{ef}) was calculated according to eq. S11

$$Q_{ef} = \frac{180° - \theta_A}{180°} \cdot 100\% \qquad \text{(S11)}$$

The reversible change in angle (θ_{rev}) was calculated by eq. S12

$$\theta_{rev} = \theta_\mathrm{A} - \theta_\mathrm{B} \qquad \text{(S12)}$$

The reversible change in concertina length (L_{rev}) was calculated by eq. S13

$$L_{rev} = L_\mathrm{A} - L_\mathrm{B} \qquad \text{(S13)}$$

Cyclic magneto-mechanical experiments were carried out with an inductor coil equipped with a tensile tester as previously described.[4] In the initial test module stretching of the test specimen ($20 \times 2 \times 1$ mm^3) to $\varepsilon = 50\%$ at $H_\mathrm{reset} = 30$ kA·m^{-1} and subsequent cooling to ambient temperature by switching the field strength to H_off was applied for programming. The reversible actuation was investigated subsequently by switching H from $H_\mathrm{off} = 0$ kA m^{-1} to $H_\mathrm{high} = 11.2$ kA·m^{-1} repeatedly under stress-free conditions and strain data with time were recorded.

Fixation efficiency Q_ef was calculated according to eq. S14

$$Q_{ef} = \frac{\varepsilon_A}{\varepsilon_{prog}} \cdot 100\% \qquad \text{(S14)}$$

The reversible elongation (ε_rev) was calculated according to eq. S15

$$\varepsilon_{rev} = \frac{\varepsilon_\mathrm{B} - \varepsilon_\mathrm{A}}{1 + \varepsilon_\mathrm{A}} \cdot 100\% \qquad \text{(S15)}$$

4.2. Remote Actuation Behavior

Magneto-mechanical tensile testing: To quantify the actuation performance of the composite, cyclic, magneto-mechanical tensile tests were conducted. In these experiments, the sample ($20 \times 2 \times 1$ mm^3) was stretched to $\varepsilon = 50\%$ at $H_\mathrm{reset} = 30$ kA·m^{-1}, and subsequently fixed by switching the field strength to H_off. The reversible actuation was investigated by switching H from H_off to H_high repeatedly under stress-free conditions and strain data were recorded. The reversible changes in elongation (ε_rev) from ε_A at H_high to ε_B at H_off were utilized for quantification of the remote actuation. The geometrical constraints of the magnetic coil, which enabled a low programming deformation of $\varepsilon_\mathrm{prog} = 50\%$, resulted in a moderate reversible actuation of $\varepsilon_\mathrm{rev} \approx 3\%$ (Figure S8).

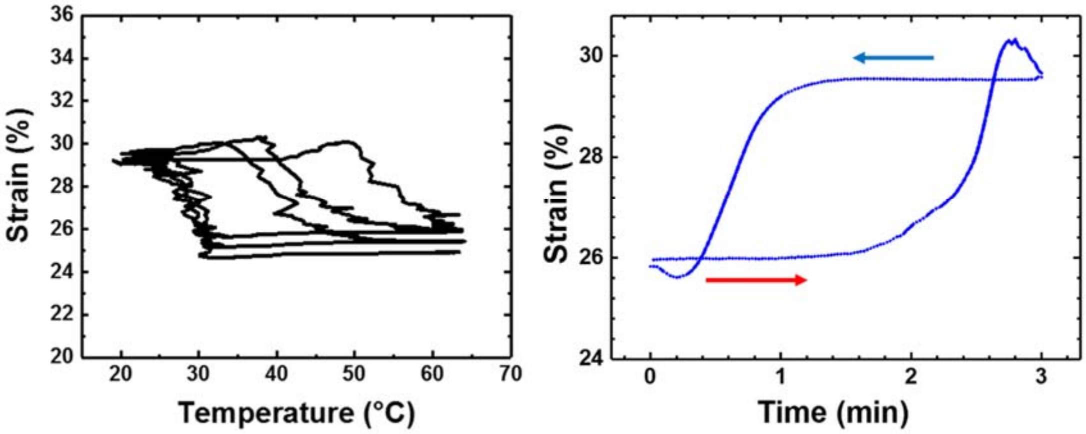

Figure S8. Changes in strain obtained in cyclic, magneto-mechanical tensile experiments of NC(85/15)-mNP-OCL.

Analysis of multicyclic magnetic actuation experiments: Most important for the actuator properties of the polymer systems is the temporal stability of the magnitude of the bending angle change during the multicycle magnetic experiment, as presented in manuscript Figure 2B. Numerical routines for peak analysis in the Origin 2017G software (OriginLab Coop., Northampton, MA, USA) were used to determine the minimum and maximum bending angles $\theta_{i,min}$ and $\theta_{i,max}$, and the respective bending angle magnitude $\Delta\theta_i = \theta_{i,max} - \theta_{i,min}$ for every cycle number i. The $\Delta\theta_i$ data are plotted as black dots in Figure S9A. The high accuracy of our nanocomposite actuator system is further documented by the narrow distribution in the histogram of individual average $\Delta\theta$-events with an average value of $\Delta\theta = 15.7\pm0.3°$ (see Figure S9B). For a more detailed analysis block averaging over 10 cycles was carried out. These values are presented as bigger red dots with a red error bar in Figure S9A characterizing the standard deviation in every block. A very stable bending angle magnitude represented by block averages of 15.7±0.1° and a mean standard deviation per block of ±0.1° was found for cycles 150 to 600, while linear regression analysis of the $\Delta\theta$ values for the first 150 cycles revealed a drift in $\Delta\theta$ of about -0.4° per 100 cycles from an initial value of about 16.3 to 15.7°.

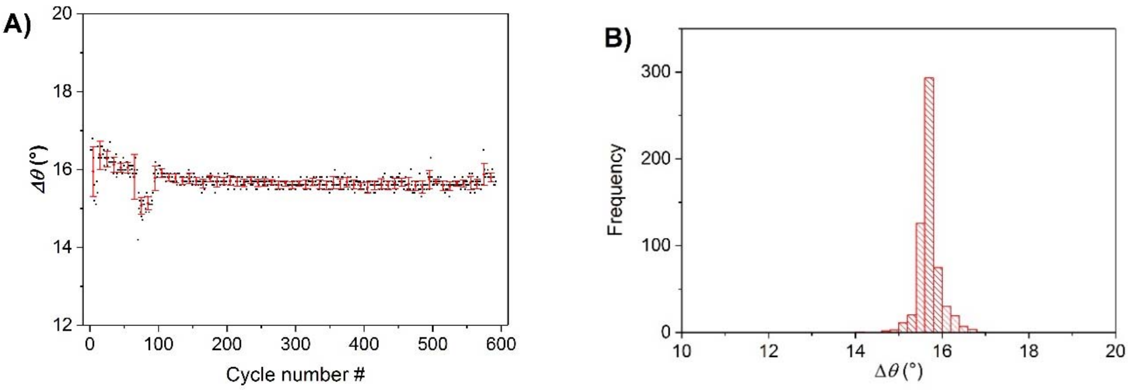

Figure S9. A) Development of the actuation performance with cycle number and B) distribution of individual average $\Delta\theta$ values.

Magnetic actuation of nanocomposite concertina: A concertina-like structure of the nanocomposite film was investigated with an iterative increase of the magnetic field strength. Here the length of the sample was determined over time and the respective field strength. Starting from an H of 9.5 kA·m^{-1} to 11.2 kA·m^{-1} a linear increase in the response is observed (Figure S10a). This increase can be explained by an increase amount of OCL domains contributing to the thermoreversible actuation.

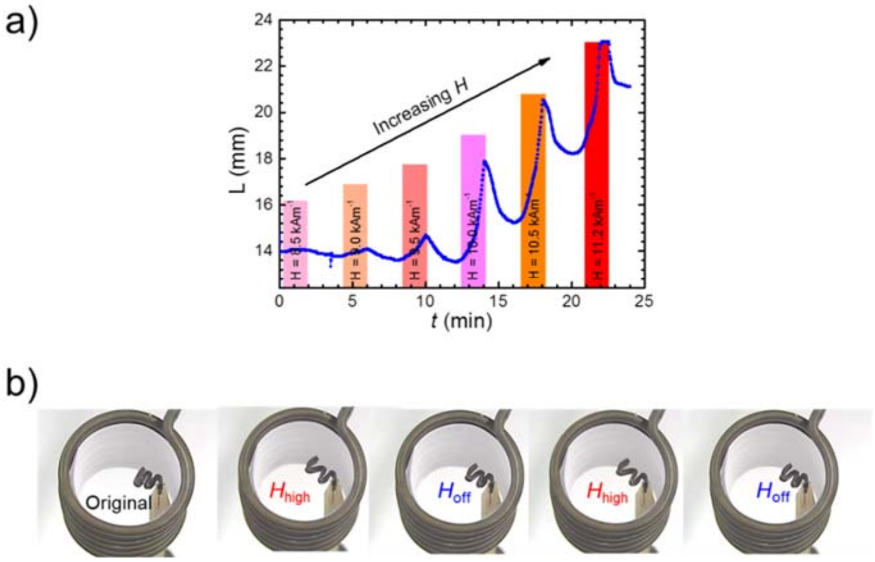

Figure S10. a) Observed changes in length (L) of a concertina-like specimen, which was reprogrammed from the sample used in the bending actuation cycles before, when exposed to AMF on-off cycles with increasing H in each subsequent cycle from H = 8.5 kA·m^{-1} to H_{high} = 11.2 kA·m^{-1}. b) Photo series showing the reversible change in the length of a concertina shaped nanocomposite during switching between H_{high} = 11.2 kA·m^{-1} and H_{off}.

Remote actuation of multi-ring device: For remote actuation of the multi-ring actuator the magnetic field strength was repetitively stepwise increased and decreased corresponding to changes in the bulk temperatures from 25 to 55 °C. Figure S11 displays the changes in the distance between the connection points of the ring structure obtained in three repetitive cycles.

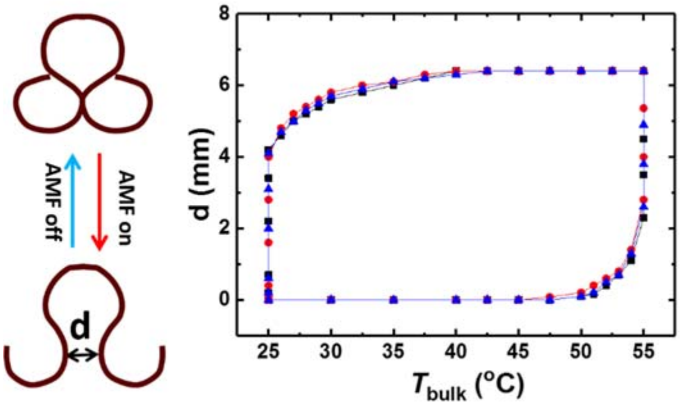

Figure S11. Observed changes in distance (*d*) of the multi-ring specimen, which was reprogrammed from the sample used in the bending actuation cycles before, when exposed to AMF on-off cycles to different T_{bulk}. Three different cycles have been performed indicated by different colors.

Table S6. Actuation properties obtained in magneto-mechanical tensile tests, rates of change in concertina length at different applied H and rates of change in bending angle at different applied H.

Cycle number	$H_{\mathbf{high}}$[a] **(kA·m^{-1})**	$Q_{\mathbf{ef}}$[b] **(%)**	$\varepsilon_{\mathbf{rev}}$[c] **(%)**
1	11.2	56±2	3.7±0.1
2	11.2	54±2	3.0±0.1
3	11.2	56±2	3.4±0.1
H **(kA m^{-1})**	$\Delta L/\Delta t$ **(mm min^{-1}) cooling step**	$\Delta L/\Delta t$ **(mm min^{-1}) heating step**	-
8.5	-0.1	0.0	-
9.0	- 0.2	0.2	-
9.5	- 0.5	0.6	-
10.0	- 1.2	2.4	-
10.5	- 1.1	2.6	-
11.2	- 1.3	2.8	-
H **(kA·m^{-1})**	$\Delta\theta/\Delta t$ **(min^{-1}) cooling step**	$\Delta L/\Delta t$ **(mm min^{-1}) heating step**	-
11.2 (cycle 1)	-10.3	-	-
11.2 (cycle 2)	- 9.2	11.9	-
11.2 (cycle 3)	- 8.1	10.5	-
10.5 (cycle 1)	- 6.1	5.3	-
10.5 (cycle 2)	- 5.3	5.3	-
10.5 (cycle 3)	- 4.9	5.5	-
10 (cycle 1)	- 4.6	3.7	-
10 (cycle 2)	- 4.4	2.9	-
10 (cycle 3)	- 4.2	3.7	-

a. Magnetic field strength used during magneto-mechanical experiments

b. Fixation efficiency of the reversible effect, see eq. S11 and S14

c. Reversible elongation, see eq. S15

5. Supporting Videos

Video S1 Description. Multi-cycle magnetically controlled actuation experiment. The nanocomposite sample (20×2×1 mm^3) was programmed by bending and subjected to 600 cycles of changes in alternating magnetic field between $H_{\mathrm{off}} = 0$ kA·m^{-1} and $H_{\mathrm{high}} = 11.2$ kA·m^{-1} with a single cycle time of 4 min. Exemplary cycles 10-16, 210-216, 410-416, and 510-516 are shown, which demonstrate the constant performance of the specimen. The video produced is in fast motion (50 times faster than real time).

Video S2 Description. Magnetically controlled actuation of a multi-ring device prepared from a nanocomposite sample with dimensions of 50×10×1 mm^3. The programmed demonstrator was fixed on a wooden stick and placed in the center of the magnetic induction coil. After the magnetic field strength H was switched to $H_{\mathrm{high}} = 11.2$ kA·m^{-1} and kept for 5 minutes the scrolled 'arms' open. When H was switched off ($H_{\mathrm{off}} = 0$ kA·m^{-1}) for further 5 minutes the scrolled ‘arms’ close again. Besides the recording the video the surface temperature was determined with an IR camera, showing the homogenous heating of the specimen as the magnetic field is turned on. Three repetitive opening and closing cycles were shown. The video shown is in fast motion (50 times faster than real time).

6. References

1. J. Zotzmann, M. Behl, Y. Feng and A. Lendlein, *Adv. Funct. Mater.*, 2010, **20**, 3583-3594.
2. L. Wang, S. Baudis, K. Kratz and A. Lendlein, *Pure Appl. Chem.*, 2015, **87**, 1085-1097.
3. L. Wang, M. Heuchel, L. Fang, K. Kratz and A. Lendlein, *J. Appl. Biomater. Funct. Mater.*, 2013, **10**, 203-209.
4. M. Y. Razzaq, M. Behl, K. Kratz and A. Lendlein, *Adv. Mater.*, 2013, **25**, 5730-5733.
5. M. J. Jenkins and K. L. Harrison, *Polym Adv. Tech.*, 2006, **17**, 474-478.
6. N. Simpson, M. Takwa, K. Hult, M. Johansson, M. Martinelle and E. Malmström, *Macromolecules*, 2008, **41**, 3613-3619.
7. L. Fang, W. Yan, U. Nöchel, K. Kratz and A. Lendlein, *Polymer*, 2016, **102**, 54-62.
8. I. Levine, R. B. Zvi, M. Winkler, A. M. Schmidt and M. Gottlieb, *Macrom. Symp.*, 2010, **291**, 278-286.
9. S. Adamovsky and C. Schick, *Thermochim. Acta*, 2004, **415**, 1-7.